ACS APPLIED MATERIALS & INTERFACES

Research Article

www.acsami.org

Phase-Field Based Multiscale Modeling of Heterogeneous Solid Electrolytes: Applications to Nanoporous Li_3PS_4

Jia-Mian Hu,* Bo Wang, Yanzhou Ji, Tiannan Yang, Xiaoxing Cheng, Yi Wang, and Long-Qing Chen

Department of Materials Science and Engineering, The Pennsylvania State University, University Park, Pennsylvania 16802, United States

Supporting Information

ABSTRACT: Modeling the effective ion conductivities of heterogeneous solid electrolytes typically involves the use of a computer-generated microstructure consisting of randomly or uniformly oriented fillers in a matrix. However, the structural features of the filler/matrix interface, which critically determine the interface ion conductivity and the microstructure morphology, have not been considered during the microstructure generation. Using nanoporous β-Li_3PS_4 electrolyte as an example, we develop a phase-field model that enables generating nanoporous microstructures of different porosities and connectivity patterns based on the depth and the energy of the surface (pore/electrolyte interface), both of which are predicted through density functional theory (DFT) calculations. Room-temperature effective ion conductivities of the generated microstructures are then calculated numerically, using DFT-estimated surface Li-ion conductivity (3.14×10^{-3} S/cm) and experimentally measured bulk Li-ion conductivity (8.93×10^{-7} S/cm) of β-Li_3PS_4 as the inputs. We also use the generated microstructures to inform effective medium theories to rapidly predict the effective ion conductivity via analytical calculations. When porosity approaches the percolation threshold, both the numerical and analytical methods predict a significantly enhanced Li-ion conductivity (1.74×10^{-4} S/cm) that is in good agreement with experimental data (1.64×10^{-4} S/cm). The present phase-field based multiscale model is generally applicable to predict both the microstructure patterns and the effective properties of heterogeneous solid electrolytes.

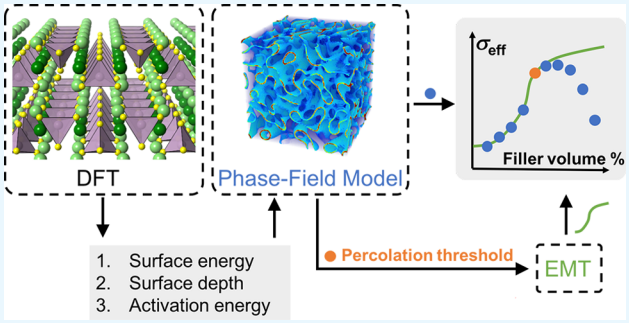

KEYWORDS: *solid electrolytes, ion conductivity, density functional theory, phase-field modeling, effective medium theory*

1. INTRODUCTION

Commercial batteries contain flammable organic liquids as electrolytes. Thus, it is unsafe to deploy them in critical energy technologies where safety is a major concern such as powering electric vehicles and stationary energy storage. Research into all-solid-state batteries that utilize nonflammable solid-state fast ion conductors as electrolytes is therefore increasing rapidly.[1−6] However, there is still no available solid electrolyte that is environmentally friendly and low-cost, has good chemical and mechanical compatibility with electrode materials, and exhibits high ion conductivity at low temperatures. Achieving all these properties simultaneously is crucial to developing a commercially viable all-solid-state battery with long cycle and shell life yet has remained a challenge.[7]

One promising solution to this challenge is to utilize heterogeneous solid electrolytes integrating two or more constituents (viz., phases, domains, and grains). A heterogeneous solid electrolyte permits the coexistence of two or more desirable properties that may not coexist in a homogeneous electrolyte, e.g., polymer (matrix)−nanowire oxides (fillers) composite electrolytes[8−11] that simultaneously have high mechanical flexibility, high ion conductivity, and good electrochemical stability. A heterogeneous solid electrolyte may also exhibit properties that are superior to their homogeneous constituents.

This work focuses on the ion conductivity of a heterogeneous solid electrolyte, using Li-ion-conducting systems as an example. A heterogeneous Li-ion-conducting solid electrolyte can be a composite of low Li-ion-conductivity matrix and second-phase fillers,[8−15] a glass ceramic containing mixed crystallites and glassy phase,[16−18] or a porous solid electrolyte containing mixed phases of solid electrolyte and air.[19] Notably, an orders-of-magnitude higher Li-ion conductivity can be achieved when fillers (more precisely, the highly ion-conductive filler/matrix interfaces[8−11,15−18]) form an interconnected (a.k.a. percolating) ion-conducting network. Note that the mechanism of the observed high ion conductivity along the interface is still an open question and may vary with specific materials.[10]

Computational models based on random-resistor-network (RRN) method[20−25] and finite element analyses[10,26] have been developed to numerically calculate the effective ion conductivity of a heterogeneous solid electrolyte with a

Received: July 30, 2017
Accepted: September 7, 2017
Published: September 7, 2017

   DOI: 10.1021/acsami.7b11292

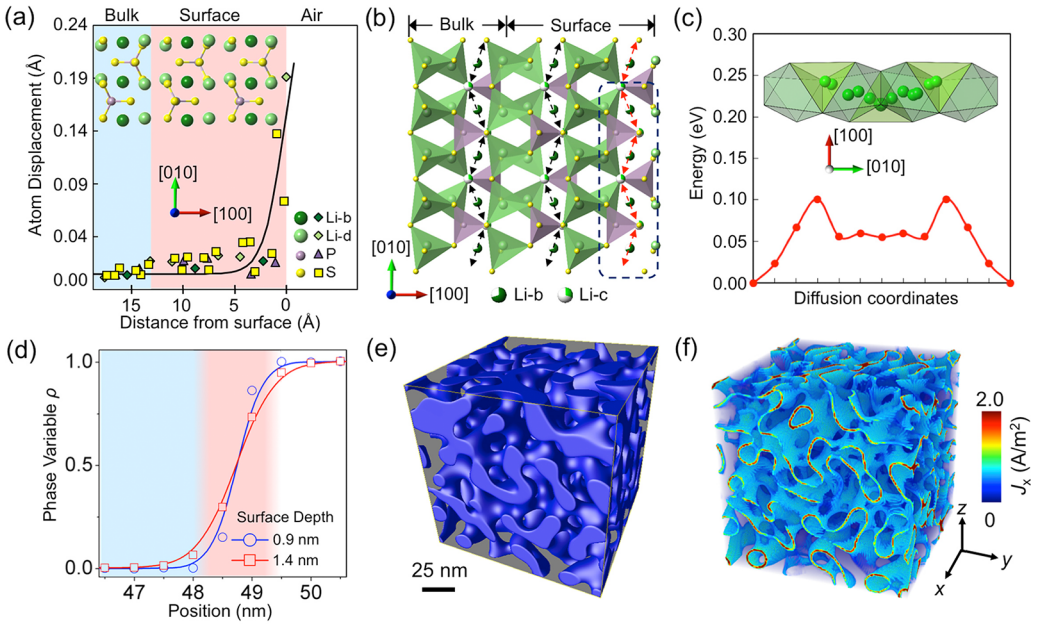

Figure 1. (a) Atom displacements along the (100) surface normal of a slab model β-Li_3PS_4 obtained through DFT calculations, using the atom coordinates in a bulk model β-Li_3PS_4 as reference. The inset shows the optimized surface structure, within only half of the three-layer slab model shown for simplicity. (b) Schematic of a zigzag Li-ion migration path in the bulk region and along the surface of a (100)-oriented β-Li_3PS_4. Note that *b*- and *c*-site Li are partially occupied in practice, providing abundant vacant sites for the Li-ion hop. (c) Energy profiles of surface Li-ion migration along the zigzag path calculated through NEB calculations, with a corresponding trajectory of Li-ion hopping between *b*-site (at the center of LiS_6 octahedrons, dark green) and *c*-site (at the center of LiS_4 tetrahedrons, light green). (d) Profiles of the phase variable across the surface of the solid electrolyte. A flatter profile indicates a larger surface depth. 3D distributions of (e) the phase variable $\rho(\mathbf{r})$ in an interconnected microstructure pattern (where blue color represents the air phase) and (f) the equilibrium current density $J_x(\mathbf{r})$ upon applying an electric field of 10 V/m along the *x*-axis.

pregenerated microstructure pattern. The structural features of the filler/matrix interface (e.g., the interface width and energy) have however not yet been considered during the microstructure generation, irrespective of their critical role in determining the interface ion conductivity and the microstructure morphology.

In this work, we develop a phase-field model that can generate 3D two-phase microstructures of different connectivity patterns by modeling the microstructure formation in phase separation. Notably, the phase-field model considers the effect of the width and the energy of the filler/matrix interface on microstructure morphology, and both interface structural features may be obtained through first-principles density functional theory (DFT) calculations. The effective ion conductivities of the generated microstructures are predicted through both numerical calculation and effective medium theories; in both cases, the DFT-estimated interface ion conductivity is used as one of the key input parameters. Using nanoporous β-Li_3PS_4[19] as an example, we employ such phase-field method based multiscale model to generate nanoporous microstructures of different porosities and connectivity patterns and predict the effective ion conductivities σ_{eff} of these microstructures.

2. METHODS

2.1. First-Principles DFT Calculations of Surface Structure, Surface Energy, and the Activation Energy of Surface Li-Ion Migration in β-Li_3PS_4. DFT[27] based first-principles calculations were performed with the Vienna ab initio simulation package.[28] The use of standard projector augmented wave (PAW) pseudopotentials[29] with local-density approximation (LDA)[30] for exchange-correlation functional was suggested[31] for modeling lithium thiophosphates by first-principles DFT calculations. Valence electron configurations of the Li, P, and S atom were chosen as $1s^22s^1$, $3s^23p^3$, and $3s^23p^4$, respectively. The plane wave cutoff energy was set as 650 eV. Convergences of energy and residual forces with respect to iterating cycles were reached when the total energy difference was less than 10^{-5} eV/atom and the forces were less than 0.01 eV/Å. A unit cell containing 32 atoms was used to optimize the lattice constants with Monkhorst–Pack[32] **k**-point meshes ($4 \times 6 \times 8$) and Gaussian smearing of 0.05 eV for the Brillouin zones sampling. For point-defects-related calculations, $1 \times 2 \times 2$ and $2 \times 2 \times 2$ supercells containing 128 and 256 atoms, respectively, were used with single **k**-point in the bulk and slab model of β-Li_3PS_4. The choice of reference ground states of Li, P, and S is based on literature.[33,34] To determine the migration paths and barriers, the nudged elastic band (NEB) method[35] was used to search for transition states. Notably, the slab model built for surface-related calculations includes an additional 10 Å thick vacuum buffer layer to reduce the interaction between the slab and its images. Moreover, the slab model is built to have mirror symmetry with respect to the central plane of the slab in order to eliminate the dipole electric field across the slab.

The crystal structure of β-Li_3PS_4 (space group *Pnma*) is complicated by the partial occupancy of Li sites, that is, the *b*- and *c*-sites (the Wyckoff notation, see schematic in Figure 1b) of Li are 70 and 30% occupied, respectively.[36] As the system size in DFT calculations is generally too small to accommodate such partial Li-occupancy, we considered two variants of crystal structure for β-Li_3PS_4 with 100% occupancy of either *b*- or *c*-site (denoted as β-Li_3PS_4-*b* and β-Li_3PS_4-*c*) based on suggestions in literature.[31,37] In both cases, the optimized lattice constants (Supporting Information S1) match perfectly with an existing DFT calculation.[31] In the present study, the β-Li_3PS_4-*b* was utilized as the reference crystal structure because it shows better structural stability (viz., more negative heat of formation).[31]

A three-layer slab model constructed from the optimized bulk lattice constants was employed to obtain the surface energy (see details in Supporting Information S2) and the optimized surface structure of β-Li_3PS_4 (see half of such three-layer slab model in the inset of Figure

1a). The present three-layer slab model is sufficiently large to eliminate the interaction of the two surfaces in the slab. As shown in Figure 1a, the atom coordinates in the leftmost layer remain almost the same as those in bulk β-Li_3PS_4 (that is, with almost zero displacements compared to bulk coordinates). For β-Li_3PS_4, our calculations show that the (100) surface with d-site Li termination (which is the most stable surface configuration)[31] has a surface energy γ of 0.020 eV/Å^2, quite close to the reported[31] theoretical value of 0.021 eV/Å^2.

2.2. Phase-Field Models for Generating 3D Material Microstructures. Phase-field modeling has been utilized to generate various types of microstructures based on the thermodynamic and kinetic principles of microstructure formation and evolution.[38] Thus, microstructures generated by phase-field modeling would typically show good consistency with experimental observations (see examples in alloys[39] and oxides[40]). Here we develop a phase-field model that enables generating different types of morphological patterns of a two-phase composite via phase separation from a homogeneous solution. In a phase-field method, the phase morphology is typically described by the spatial distribution of a continuous phase variable $\rho(\mathbf{r})$. For a nanoporous microstructure, $\rho(\mathbf{r})$ represents the relative mass density of each constituent phase, where ρ equals 0 in the pore phase, 1 in bulk solid phase, and varies continuously from 0 to 1 at the solid surface (see Figure 1d). Such a diffuse-interface description is the main feature of the phase-field method. The diffuse-interface description is based on the fact that all interfaces at finite temperatures have a finite thickness. In this work, the thickness of the surface depth is carefully determined based on the DFT calculations. The rationale behind the adoption of such diffuse-interface description is discussed in refs 41 and 42. In the framework of such diffuse-interface theory,[41,43] the total free energy F of such a heterogeneous system is expressed as a function of $\rho(\mathbf{r})$ and its gradient:

$$F = \int_V \left(f_{\text{chem}}(\rho) + \frac{1}{2}\kappa_{ij}(\nabla_i\rho)\,(\nabla_j\rho) \right) \mathrm{d}V \tag{1}$$

where f_{chem} is the bulk chemical free energy density (in the unit of J/m^3) and κ_{ij} is the gradient energy coefficient (J/m). To describe phase separation, a double-well type free-energy function is typically employed for f_{chem} such that the global energy minima appear at $\rho = \rho_s = 1$ and $\rho = \rho_p = 0$:[44]

$$f_{\text{chem}}(\rho) = \frac{16w}{(\rho_s - \rho_p)^4}(\rho - \rho_s)^2(\rho - \rho_p)^2 \tag{2}$$

Note that both the gradient energy coefficient κ and the energy density barrier w (J/m^3) between the two energy minima are determined by the surface energy (γ) and surface depth (λ), and for a 1D system, we have analytical expressions given by $\kappa = (3/2)\gamma\lambda$ and $w = (3/4)(\gamma/\lambda)$ when $\rho = 0.1$ and 0.9 at the two ends of the surface depth. In this study, both γ and λ were informed by DFT calculations (see previous section), with $\gamma = 0.020$ eV/Å^2 and λ ranging approximately from 1.0 to 1.5 nm (see Figure 1a). To investigate the influence of the surface depth, λ of two different values (0.9 and 1.4 nm) were utilized.

We then modeled the microstructure evolution during phase separation by solving the Cahn–Hilliard equation:[45]

$$\frac{\partial\rho}{\partial t} = \nabla\left(M(\rho)\,\nabla\left(\frac{\partial f_{\text{chem}}}{\partial\rho} - \kappa_{ij}\nabla_i\nabla_j\rho \right) \right) \tag{3}$$

Here $M(\rho)$ is a spatially variant mobility (in the unit of m^2/ (J·s)) given by

$$M(\rho) = (1 - a^2(\rho - \rho_s) + (\rho - \rho_p))^2(M_p(\rho - \rho_p) + M_s(\rho_s - \rho)) \tag{4}$$

where M_p and M_s are the mobility of two diffusive species, a ($0 \le a \le 1$) is a parameter determining whether the phase separation process is controlled by bulk diffusion ($a = 0$) or interface diffusion ($a = 1$).[45,46] For simplicity, we consider a constant diffusion mobility $M(\rho) = M_s$, which is estimated from the DFT-calculated self-diffusion coefficient of Li-vacancy D_v. Equation 3 was numerically solved with a semi-implicit Fourier-spectral algorithm[45,46] in a discretized 3D periodic system with a dimension of $256l_0 \times 256l_0 \times 256l_0$. The grid size $l_0 = 0.5$ nm is small enough to resolve the DFT-calculated surface depth λ. A near-equilibrium microstructure is obtained when $\partial\rho/\partial t \approx 0$.

Tuning the relative ratios of the three diagonal components of κ_{ii} (i = 1, 2, and 3) enables generating filler/matrix microstructures of different connectivity patterns. Specifically, we fix the κ_{33} to $(3/2)\gamma\lambda$ (see text below eq 2), while tuning the κ_{11} and κ_{22}, with $\kappa_{11} = \kappa_{22} = \kappa_{33}$ and $10\kappa_{11} = 10\kappa_{22} = \kappa_{33}$ in Figures 2a and 3a, respectively, and with

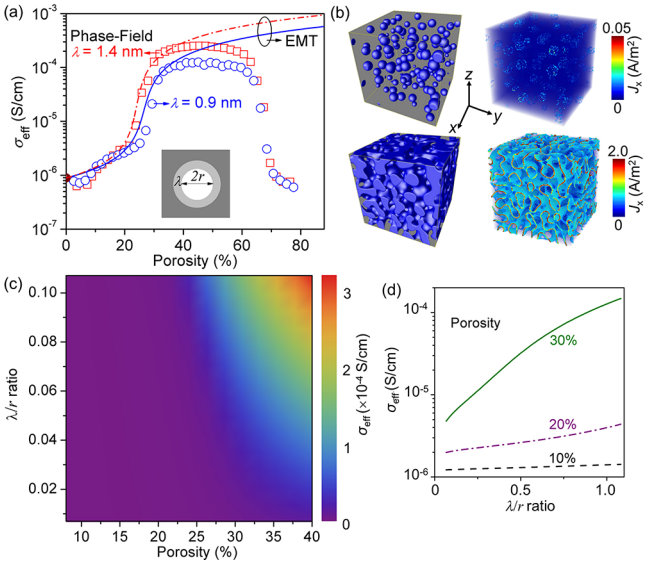

Figure 2. (a) Effective ion conductivities $\sigma_{\text{eff}} = [(\sigma_{xx} + \sigma_{yy} + \sigma_{zz})/3]$ of nanoporous β-Li_3PS_4 as a function of porosity and surface depth λ, calculated numerically on the basis of microstructure patterns generated by phase-field simulations (open symbols) and analytically by effective medium theory (EMT) calculations (lines). In phase-field simulations, 3D surface-ion-conducting networks form when porosity exceeds the first percolation threshold (~32%). To reduce possible statistic errors, the σ_{eff} at each value of porosity was calculated from five different microstructure patterns and then averaged out. The EMT calculations do not consider an actual microstructure pattern, yet assumes a matrix with core (air)-shell (surface) spherical fillers that are well-separated and uniform in radius r (= 14 nm, see inset). (b) Microstructure patterns and distributions of equilibrium current density $J_x(\mathbf{r})$ in a 5.4% porosity (the first row) and a 43.5% porosity (the second row) electrolyte. A 10 V/m electric field is applied along the x-axis. (c) Map of the σ_{eff} under a range of porosities and λ/r ratios calculated using EMT, and (d) corresponding line profiles at selected porosities.

κ_{11}/κ_{33} and κ_{22}/κ_{33} varying from 0.5 to 6000 in Figure 4a,b. Here we term κ_{11}/κ_{33} and κ_{22}/κ_{33} as shape factors x and y, respectively, because the equilibrium shape of a filler can be determined through Wulff's construction[47] if these two ratios are known. Specifically, the filler should be (i) sphere-shaped when $\kappa_{11} \approx \kappa_{22} \approx \kappa_{33}$, (ii) rod-shaped when $\kappa_{22} \approx \kappa_{33} \ll \kappa_{11}$ (along x), $\kappa_{11} \approx \kappa_{33} \ll \kappa_{22}$ (along y), or $\kappa_{11} \approx \kappa_{22} \ll \kappa_{33}$ (along z), and (iii) laminated when $\kappa_{33} \ll \kappa_{11} \approx \kappa_{22}$ (xy-plane), $\kappa_{22} \ll \kappa_{11} \approx \kappa_{33}$ (xz-plane), or $\kappa_{11} \ll \kappa_{22} \approx \kappa_{33}$ (yz-plane). Phase-field simulations supported such expectations (see Figure 4c).

In a filler/matrix (porous) microstructure formed by phase separation, the equilibrium volume fraction of the fillers (porosity) is linearly proportional to the relative density of the initial supersaturated homogeneous solution ρ_0 ($0 \le \rho_0 \le 1$). Thus, the microstructures with increasing porosity (Figures 2a and 3a) can be obtained by increasing ρ_0. Depending on the value of ρ_0, kinetic pathways of phase separation would either be spinodal decomposition or nucleation-and-growth. The critical values of ρ_0 separating these two pathways were obtained to be about 0.21 and 0.79 by solving

DOI: 10.1021/acsami.7b11202

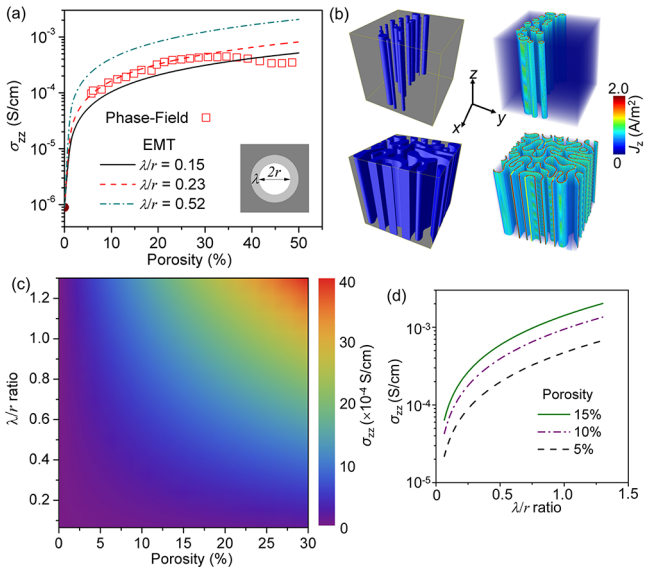

Figure 3. (a) Effective ion conductivities σ_{zz} of β-Li_3PS_4 as a function of porosity, calculated numerically on the basis of microstructure patterns (matrix with hollow nanopillars orienting along the z-axis) generated by phase-field simulations (open symbols) and analytically by effective medium theory (EMT) calculations (lines). The hollow nanopillars enables the formation of 1D surface-ion-conducting channels. In phase-field simulations, the σ_{eff} at each value of porosity was calculated from five different microstructure patterns and then averaged out for reducing possible statistics errors. The EMT calculations were performed by assuming a matrix with core (air)−shell (surface) pillars of different radii r (see inset). (b) Microstructure patterns and distributions of equilibrium current density $J_z(\mathbf{r})$ in a 6.1% porosity (the first row) and a 48.7% porosity (the second row) electrolyte. A 10 V/m electric field is applied along the z-axis. (c) Map of the σ_{eff} under a range of porosities and λ/r ratios calculated using EMT, and (d) corresponding line profiles at selected porosities.

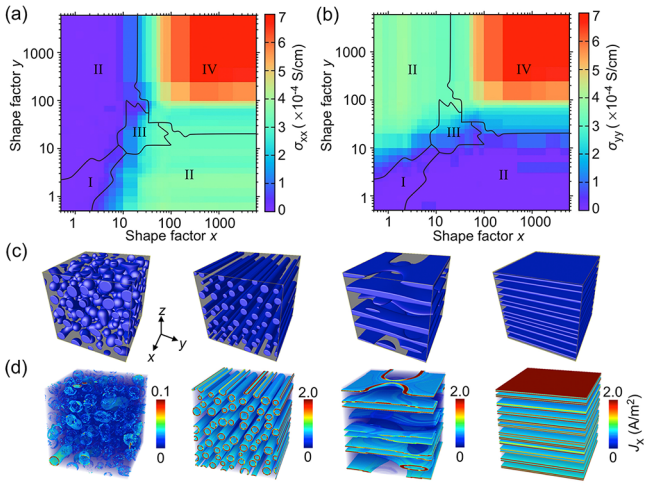

Figure 4. (a, b) Phase diagrams showing the phase connectivity of 1600 different two-phase microstructure patterns generated by phase-field modeling, as well as the numerically calculated effective ion conductivity σ_{xx} and σ_{yy}. (c) Microstructure patterns generated (from left to right) using the shape factors of (x, y) = (1,1), (3000,1), (20,20), and (3000, 3000) that have 0−3, 1−3, 2−3, and 2−2 type connectivity, respectively. (d) Their corresponding equilibrium current densities $J_x(\mathbf{r})$ upon applying an electric field of 10 V/m along the x-axis.

$\partial^2 f_{chem}/\partial\rho^2 = 0$. Specifically, when $0.21 \le \rho_0 \le 0.79$ (inside spinodal), random noises were added to trigger phase separation because the initial supersaturated homogeneous solution is unstable with respect to any small fluctuations in density. When $\rho_0 < 0.21$ or $\rho_0 > 0.79$, the initial supersaturated solution is metastable; a nucleation barrier needs to be overcome to trigger phase separation. In those metastable regimes, nucleation sites (in which $\rho = 0$ or 1) were explicitly added into the solution, and classical nucleation theory was employed to determine the nucleation rate j:

$$j = N \exp\left(\frac{\Delta G^*}{k_B T}\right) \tag{5}$$

where N is the total number of nucleation sites, k_B is the Boltzmann constant (in the unit of J/K), T the Kelvin temperature (K), and ΔG^* is the energy barrier for nucleation (J). Assuming a spherical nucleation site yields $\Delta G^* = (16\pi\gamma^3)/3(\Delta g_v)^2$, where Δg_v represents the driving force for nucleation in the energy landscape of f_{chem}. Poisson seeding was utilized to determine the nucleation probability p in each discretized grid at each time step:[48]

$$p = 1 - \exp(-j\Delta t) \tag{6}$$

where Δt is the time step size. To ensure mass conservation (i.e., $\langle\rho(\mathbf{r})\rangle$ equals ρ_0, where the angular brackets indicate the volume average), the relative densities outside the nuclei regions were adjusted in a similar manner to the treatment in ref 44.

2.3. Numerical Calculation of Effective Ion Conductivity. The local Li-ion conductivity $\sigma(\mathbf{r})$ of a phase-field generated microstructure is related to $\rho(\mathbf{r})$, specifically, $\sigma = 0$ when $\rho < 0.1$, $\sigma = \sigma_{bulk} = 8.93 \times 10^{-7}$ S/cm (from experiments)[19] when $\rho > 0.9$, and $\sigma = \sigma_{surf} = 3.14 \times 10^{-3}$ S/cm (estimated through DFT calculations) within the surface depth ($0.1 \le \rho \le 0.9$). The effective Li-ion conductivity σ_{eff} is given by $\sigma_{eff} = \langle J(\mathbf{r})\rangle/E$. The distribution of local current density $J(\mathbf{r})$, in the unit of A/m^2, was obtained by solving a steady-state current conduction equation under an applied static electric field E (V/m),

$$\nabla\cdot J(\mathbf{r}) = \nabla\cdot[\sigma(\rho)E] = 0 \tag{7}$$

Equation 7 was numerically solved using a Fourier spectral iterative perturbation method.[49,50]

2.4. Analytical Calculation of Effective Ion Conductivity through EMT. Effective medium theories (EMT) have been utilized to calculate the σ_{eff} of composite solid electrolytes since the late 1970s.[51−55] Although EMT do not consider an actual microstructure, the features of a computationally generated (or experimentally measured) microstructure can normally inform the EMT for a better prediction of the material properties. Here, the nanoporous Li−S electrolyte is equivalent to a three-phase composite of a low-conductivity Li_3PS_4 matrix, air (fillers), and their highly conductive interfaces. The Li-ion conductivities in these phases are denoted as σ_m, σ_f, and σ_s, respectively. We extend the generalized EMT (GEMT)[56] that was developed for two-phase composites to three-phase composites based on suggestions of Nan et al.[52,54] Such extension is made possible by treating the three-phase composite as a composite particle, consisting of a spherical core (the air, with a diameter $2r$) and a highly conductive shell (the surface, with a depth λ), embedded in a matrix (Li_3PS_4), as sketched in the inset of Figure 2a. Specifically, we first calculate the effective ion conductivity of the composite particle σ_c using a simple parallel brick-layer model[57−59] (i.e., $\sigma_c = g_f\sigma_f + (1 - g_f)\sigma_s$, where $g_f = 1/(1 + \alpha)^3$ represents the volume fraction of the air core in the composite particle, with $\alpha = \lambda/r$). The effective ion conductivity of the three-phase composite σ_{eff} can then be calculated using classical GEMT.

For a nanoporous Li−S electrolyte with 3D ion-conducting network above percolation threshold (e.g., see Figures 1e and 2b), its σ_{eff} can be calculated by assuming that the pores are spherical, well-separated, and uniform in diameter:

$$\left(\frac{g}{g_f}\right)\frac{\sigma_c^{1/t}-\sigma_{eff}^{1/t}}{\sigma_c^{1/t}+\left(\frac{1}{p_{c1}}-1\right)\sigma_{eff}^{1/t}}+\left(1-\frac{g}{g_f}\right)\frac{\sigma_m^{1/t}-\sigma_{eff}^{1/t}}{\sigma_m^{1/t}+\left(\frac{1}{p_{c1}}-1\right)\sigma_{eff}^{1/t}}=0 \quad (8)$$

where g represents the volume fraction of the air core in the entire three-phase composite, p_{c1} is the first percolation threshold that can be obtained from the interconnected microstructure patterns generated through phase-field simulations (~0.32, see Figure 2a), and t is an effective percolation slope[55] that can be tuned to fit the phase-field simulation results (taken as 0.85 for results in Figure 2a). In doing so, the phase-field simulations inform the EMT calculations. For a vertical nanostructure with 1D ion-conducting channels along the z-axis, the effective ion conductivity σ_{zz} can be directly calculated using the parallel brick-layer model (i.e., $\sigma_{zz} = (g/g_f)\sigma_c + [1-(g/g_f)]\sigma_m$, where $g_f = 1/(1+\alpha)^2$ in this case). Note that the value of α ($= \lambda/r$) can also be obtained from the vertical microstructure patterns generated through phase-field simulations (Figure 3b).

3. RESULTS AND DISCUSSIONS

The Li-ion conductivity in a nanoporous β-phase Li_3PS_4 has been experimentally observed[19] to be over 2 orders of magnitude larger than that in a bulk β-Li_3PS_4. The authors attributed this enhancement to the porous sample's large surface areas, in which ion conductivity can be higher than that in bulk region due to ion-accumulation space-charge effect,[60] yet the possibility of forming a 3D percolating ion-conducting network based on these highly conductive surfaces was not discussed. Here we computationally test this possibility by developing a phase-field model (Methods) to generate nanoporous solid electrolytes of different microstructure patterns and predict their corresponding effective ion conductivity σ_{eff}. All the input parameters required by the phase-field model to predict σ_{eff} were obtained from first-principles DFT calculations (Methods) or existing experiments.

Figure 1a shows the magnitudes of displacements of Li, P, and S atoms along the (100) surface normal of a slab model β-Li_3PS_4 away from their coordinates in bulk β-Li_3PS_4. Relatively significant surface relaxation occurs roughly within the first 1.5 nm (namely, the surface depth λ). Notably, the outermost d-site Li moves inward (i.e., along $[\bar{1}00]$) by 0.2 Å. Such structural variance at the surface should result in ion-conducting behaviors that are different from those in bulk. Previous first-principles DFT calculations[31,37] and experiments[61] have suggested that bulk Li-ion migration in β-Li_3PS_4 preferably follows a zigzag path along the [010] axis (see Figure 1b) along which there are abundant vacant b- or c-type Li-sites due to intrinsic partial Li-occupation. Our NEB calculations indicate that the surface Li-ion migration preferably follows a similar path (see Supporting Information S3). With this knowledge, we further use first-principles DFT calculations to estimate the surface Li-ion (vacancy) conductivity σ_{surf}, which is a critical input parameter for subsequent phase-field modeling. In general, the ion conductivity σ_k of a defect k can be obtained from the Nernst–Einstein equation:[62]

$$\sigma_k = \frac{z_k^2 F^2 c_k D_k}{RT} \quad (9)$$

where z_k, c_k, and D_k denote the charge number (dimensionless), concentration (in the unit of mol/m^3), and self-diffusion coefficient (m^2/s) of a defect, respectively; F and R are the Faraday constant (C/mol) and ideal gas constant (in the unit of J/ (mol·K)), respectively; and T is the Kelvin temperature (K). For the β-Li_3PS_4 with Frenkel defects (pairs of Li vacancies V'_{Li} and interstitials $Li_i^{\cdot}$), the self-diffusion coefficient of a Li vacancy D_v can be obtained based on classical atomic theory of diffusion:[63]

$$D_v = \gamma a^2 \nu \exp\left(\frac{\Delta S_{m,v} + \Delta S_f/2}{k_B}\right)\exp\left(-\frac{\Delta H_{m,v} + \Delta H_f/2}{k_B T}\right) \quad (10)$$

where γ, a, and ν are the geometric factor (dimensionless), lattice parameter (in the unit of m), and lattice vibration frequency (ca. the Debye frequency, in the unit of Hz), respectively, $\Delta S_{m,v}$ ($\Delta H_{m,v}$) is the vacancy migration entropy (enthalpy), in the unit of J/K (J), while ΔS_f (ΔH_f) is the formation entropy (enthalpy) of the V'_{Li}–$Li_i^{\cdot}$ defect pair. Given that the Li vacancy concentration c_v is proportional to $\exp(\Delta S_f/2k_B)\exp(-\Delta H_f/2k_BT)$, the vacancy conductivity σ_v can be written as

$$\sigma_v = \sigma_0 \exp\left(\frac{\Delta S_{m,v} + \Delta S_f}{k_B}\right)\exp\left(-\frac{\Delta H_{m,v} + \Delta H_f}{k_B}\right);\quad \sigma_0 \propto \frac{\gamma a^2 \nu z^2 F^2}{RT} \quad (11)$$

We expect that the geometric factor γ might be slightly larger at the surface, because surface Li-ion diffusion generally behaves like a 2D diffusion ($\gamma = 1/4$) or even a 1D diffusion if there is a unidirectional migration path ($\gamma = 1/2$) rather than 3D (e.g., $\gamma = 1/6$ in an isotropic 3D system). Moreover, the lattice parameter a at the surface is also similar to its bulk value (see Figure 1a). The lattice vibration frequency ν, which is related to the speed of sound and the density of atoms in the solid, should not have orders of magnitude difference between the surface and the bulk. The vacancy migration ($\Delta S_{m,v}$) and formation (ΔS_f) entropy terms are both contributed by a vibrational term ΔS_{vib} that is related to the vibration frequency ν, and a configurational term ΔS_{conf} that is related to the Li-ion site occupancy.[64] Notably, it has been suggested[64] that the ΔS_{vib} should directly depend on the ΔS_{conf} and that the Li-ion site occupancy varies strongly with local composition and temperature. Here we assume that the local composition at the bulk and surface region of the β-Li_3PS_4 remains largely the same; thereby, the ΔS_{conf} should not have a sizable difference. Taken together, the expected orders of magnitude enhancement in the surface Li-ion conductivity[10,19] should be mainly determined by the activation energy of ion migration $Q = \Delta H_{m,v} + \Delta H_f$. In this regard, the surface Li-ion (vacancy) conductivity σ_{surf} can be estimated as

$$\sigma_{surf} \approx \sigma_{bulk} \exp\left(\frac{Q_{bulk} - Q_{surf}}{k_B T}\right) \quad (12)$$

where Q_{bulk} and Q_{surf} are the activation energy for bulk and surface Li-ion migration in β-Li_3PS_4, respectively. As the experimentally measured values of room-temperature (25 °C) bulk Li-ion conductivity σ_{bulk} (8.93×10^{-7} S/cm)[19] and corresponding Q_{bulk} (0.47 eV)[65] are available, the unknown parameters are the ΔH_f and $\Delta H_{m,v}$ for the surface Li-ion migration. For estimating these two parameters, let us consider a defect pair of b-site V'_{Li} and c-site $Li_i^{\cdot}$ in the zigzag path at the surface (highlighted by dashed square in Figure 1b). First, the formation enthalpy of the defect pair is negligibly small at the surface ($\Delta H_f \approx 0$) because the intrinsic partial Li-occupancy produces abundant Li vacancies at the b- and c-sites and

because the space-charge zone can enhance the Li-vacancy concentration at the surface.[60] Second, the surface Li-vacancy migration enthalpy $\Delta H_{m,v}$ is about 0.10 eV as seen from Figure 1c, which plots the energy profile of Li-ion (vacancy) migration along the zigzag path calculated through the NEB method. The calculated zigzag Li-migration path depicts the hopping movement of *b*- or *c*-site Li ions to neighboring vacant sites. Notably, the calculated Q_{surf} ($\approx 0 + 0.10$ eV) is lower than the Q_{bulk} calculated for a zigzag migration path in bulk region (~0.18 eV, see Supporting Information S3). We, however, utilize the experimentally measured Q_{bulk} (0.47 eV) and room temperature σ_{bulk} as well as a scaled Q_{surf}*($= kQ_{surf} \approx 0.26$ eV) to estimate the room temperature σ_{surf} through eq 12. Here the scaling factor k (≈ 2.61) is introduced to compromise the typically underestimated Q in both the previous[31,37] and the present DFT calculations on β-Li_3PS_4, and was approximated as the ratio of the experimental Q_{bulk} (0.47 eV) to our calculated one (0.18 eV). As a result, the room-temperature σ_{surf} is estimated (eq 12) to be 3.14×10^{-3} S/cm, 4 orders of magnitude larger than σ_{bulk}. In practice, the degree of partial Li-occupancy may vary locally in a 3D microstructure due to for example the variations of local composition, which would affect not only the local configuration entropy term ΔS_{conf} but also the local activation energy Q. This will lead to local variations of the σ_{surf} and the σ_{bulk}, which, however, are not likely to have orders of magnitude difference under a fixed temperature. For simplicity, here we assume that the σ_{surf} (σ_{bulk}) remains the same at different local surface (bulk) regions in nanoporous structures of different porosities.

Next, we perform phase-field simulations (Methods) to generate a 3D nanoporous microstructure that possess percolating surfaces of different depth λ and to calculate the σ_{eff} based on the σ_{surf} estimated via DFT calculations and the experimentally measured σ_{bulk}. Figure 1d shows the profiles of a phase variable $\rho(\mathbf{r})$ that change continuously from the solid electrolyte phase ($\rho = 1$) to the air phase ($\rho = 0$) across the solid surface ($0 < \rho < 1$), where two different surface depths λ are assumed. The 3D spatial distributions of $\rho(\mathbf{r})$ represent the microstructure of the nanoporous electrolytes. Figure 1e presents one example of 3D percolating nanoporous microstructures constructed using $\lambda = 1.4$ nm, where the blue color represents the air phase (porosity $\approx$ 32%). In particular, the average pore size is roughly 40 nm, which is not far from the experimental observation[19] of 28 nm in nanoporous β-Li_3PS_4. Figure 1f shows the distribution of local current densities $J_x(\mathbf{r})$ upon applying an electric field of 10 V/m along the *x*-axis, which directly illustrates the significantly enhanced $J_x(\mathbf{r})$ at the highly conductive surfaces and a 3D percolating ion-conducting network formed by these surfaces. Moreover, the effective ion conductivity $\sigma_{xx} = \langle J_x(\mathbf{r})\rangle/E_x$ of the microstructure is about 1.76×10^{-4} S/cm. σ_{yy} and σ_{zz} were calculated to be 1.72×10^{-4} and 1.75×10^{-4} S/cm, respectively, leading to an average σ_{eff} of about 1.74×10^{-4} S/cm. The fact that the calculated σ_{xx}, σ_{yy}, and σ_{zz} are similar demonstrates that the corresponding 3D percolating microstructure (Figure 1e) is structurally isotropic.

We further utilize phase-field simulations to generate nanoporous microstructure of different surface depths λ (0.9 and 1.4 nm) and different porosities (around 3−77%) and to calculate their σ_{eff} (see open symbols in Figure 2a). The phase-field simulation results reveal three messages. First, two percolation thresholds appear. Above the first threshold (ca. 32%), the highly conductive surfaces form a 3D percolating ion-conducting network; see corresponding microstructure and $J_x(\mathbf{r})$ distribution in Figure 1e,f. As a result, the σ_{eff} increases rapidly around the first threshold. Above the second threshold (ca. 61%), the β-Li_3PS_4 solid electrolyte fails to form a 3D percolating backbone. Thus, the surfaces are no longer interconnected, leading to a rapid decrease of the σ_{eff}. When porosity exceeds 77%, the β-Li_3PS_4 backbone would collapse. Such presence of two percolation thresholds at low and high porosity is analogous to the two percolation thresholds appearing at low and high volume fractions of insulating solid-state fillers in composite electrolytes (see for example refs 21 and 53). Second, the σ_{eff} (1.74×10^{-4} S/cm) at the first percolating threshold is close to the experimental data (1.64×10^{-4} S/cm). Thus, it is rational to assume the formation of 3D percolating surfaces to be the physical principle behind the experimental observation.[19] Third, the σ_{eff} in a very low-porosity sample (i.e., below a critical value of around 8% herein) is smaller than that in a dense solid electrolyte (solid symbols in Figure 2a) because the surfaces-enabled conductivity enhancement is outweighed by the volume loss-enabled conductivity decrease. Figure 2b shows the microstructure and the corresponding $J_x(\mathbf{r})$ distribution in samples with 5.4% porosity (the first row) and 43.5% porosity (the second row).

EMT were also employed to interpret the phase-field simulation results. Using the first percolation threshold from phase-field simulations (denoted as p_{c1}, ~32%) as the input, the σ_{eff} calculated by EMT (see details in the Methods) are plotted in Figure 2a (the lines) for comparison. First, as seen in both the phase-field simulations and EMT calculations, a larger surface depth λ leads to an appreciably larger σ_{eff} when the porosity exceeds a certain value (~26%), and such discrepancy increases with increasing porosity. Second, the σ_{eff} calculated by these two methods are reasonably consistent when the porosity is between 8 and 40% in both values of λ. This consistency allows us to use EMT to rapidly obtain how the surface depth, more generally the λ/r, on the σ_{eff} when porosity is between 8 and 40%, as shown in Figure 2c. Here, λ/r varies from 0.007 ($\lambda \approx 0.1$ nm) to 0.107 ($\lambda \approx 1.5$ nm). Clearly, increasing λ/r (larger surface depth or/and smaller pore size) yields a nonlinear increase in the σ_{eff} at a porosity near p_{c1} (see Figure 2d). Note that EMT, however, cannot correctly predict the variation trend of σ_{eff} at relatively low (below 8%) and high (above 40%) porosity. This is mainly because the present EMT calculations assume that the fillers are spherical (see inset in Figure 2a), well-separated, and uniform in size, whereas the phase-field simulations consider an actual microstructure that forms through phase separation; thereby, the fillers would become interconnected at high volume fractions to reduce overall interface energy.

In addition to microstructures with a 3D Li-ion-conducting network (Figures 1e and 2b), phase-field simulations can also generate microstructures with a 1D Li-ion conducting channel (Methods), for example, a matrix with second-phase pillars (pores) penetrating along one Cartesian axis, where the ion conductivity can be enhanced along that axis. Such microstructures have been fabricated experimentally via self-assembly (one type of phase separation),[66,67] lithographical patterning[10] and other types of template.[11] The open symbols in Figure 3a show the numerically calculated effective ion conductivity σ_{zz} ($= \langle J_z(\mathbf{r})\rangle/E_z$, with $E_z = 10$ MV/m) of these microstructures. As seen, introducing a small amount (e.g., 6.1%) of vertical hollow nanopillars to a dense β-Li_3PS_4 can significantly enhance the σ_{zz}. Thus, introducing 1D pillars is a more efficient strategy

DOI: 10.1021/acsami.7b11202

than introducing 3D percolating network in enhancing the ion conductivity along one desirable orientation, as demonstrated in a recent experiment.[10] The first and second row in Figure 3b show the microstructure and corresponding $J_z(\mathbf{r})$ distributions of two samples with porosity of about 6.1 and 48.7%, respectively, where the significantly enhanced $J_z(\mathbf{r})$ at the vertical surfaces clearly demonstrates a high local σ_{zz}.

Figure 3a also shows the σ_{zz} calculated through EMT under different ratios of λ/r (see inset and the Methods section). Notably, the EMT calculations using $\lambda/r = 0.23$ agree well with the phase-field-method simulated σ_{zz}. Note that phase-field simulations inform the EMT calculations; 0.23 is the average value of the λ/r in all low-porosity (below 35%) microstructure patterns generated by phase-field modeling. Similarly, we use EMT to rapidly obtain the diagram of the σ_{zz} as a function of the porosity and the λ/r (see Figure 3c, and selected line profiles in Figure 3d). Comparing Figures 3c and 2c, the effective conductivity of a microstructure with well-aligned 1D ion-conducting channels is roughly 1 order of magnitude larger than those with 3D ion-conducting network along the aligning orientation. This finding is consistent with recent experimental finding.[10] Note that the EMT calculations deviate from the phase-field simulations when the porosity of microstructures exceeds 35%. In those cases, different pillars start to merge to reduce interface energy in phase-field generated microstructure patterns but remain well separated in EMT. As a result, the volume fraction of the vertical surfaces decreases; thereby, the σ_{zz} starts to decrease until the vertical surface volume fraction starts to increase again at relatively high porosity (see Supporting Information S4 for the plot of surface volume fractions against porosity).

We now discuss how the morphological pattern of phases determines the effective ion conductivity σ_{eff} in not just the nanoporous β-Li_3PS_4 but in general a heterogeneous solid electrolyte consisting of a low-conductivity matrix, insulating second-phase fillers, and their highly conductive interfaces. Examples include low-conductivity polymer electrolyte matrix (such as poly(ethylene oxide)-based polymer, $\sim 10^{-8}$ S/cm)[68] and insulating inorganic fillers (e.g., SiO_2,[15,69] Al_2O_3,[12,70] TiO_2,[71] or ZrO_2).[72] We first perform phase-field simulations (by tuning the shape factors; Methods) to generate a data set consisting of 1600 different 3D two-phase microstructure patterns (i.e., 1600 different 3D distributions of the phase variable $\rho(\mathbf{r})$) that all have a similar filler volume fraction of about 19% (i.e., the volume average of $\rho(\mathbf{r})$ is about 19%). We then evaluate their σ_{eff} by solving eq 7. The generated 1600 3D microstructures show four different types of connectivity patterns, including 0−3, 1−3, 2−3, and 2−2 (based on the notation introduced by Newnham et al.[73]), denoted as phases I−IV, respectively, in Figure 4a,b. The type of connectivity pattern in each microstructure is evaluated explicitly by plotting the corresponding distribution of $\rho(\mathbf{r})$ in 3D. Taking the 0 (filler)−3 (matrix) connectivity as an example, "0" indicates that the fillers cannot penetrate the sample in any one Cartesian axis, while "3" indicates the matrix phase penetrates the sample in all three Cartesian axes. Note that two-phase microstructures of 3−3 connectivity (e.g., the 3D percolating nanostructure in Figures 1e and 2b) do not appear in the present phase diagrams because the filler volume fraction is far below the 3D percolation threshold (~32%). We further note that these generated microstructures can all be synthesized if the filler is in solid-state because microstructures with 0−3, 1−3, and 2−2 type connectivity patterns have already been synthesized[10,11,74] and because the 2−3 type microstructure can in principle be synthesized through for example additive manufacturing.[75] If the filler is gaseous, then only microstructures of the multilayered 2−2 type connectivity pattern cannot be synthesized.

The color backgrounds of the phase morphology diagrams in Figure 4a,b represent the effective ion conductivities σ_{xx} and σ_{yy} of these 3D microstructures, respectively. Figure 4c,d further show the typical microstructures of the four different connectivity patterns and their corresponding $J_x(\mathbf{r})$ distributions upon applying an electric field of 10 V/m along the x-axis. Specifically, a 1−3 type microstructure with rod-shaped second-phase fillers aligning along the x-axis (see the second image in Figure 4c) exhibits a high σ_{xx} ($\approx 3.41 \times 10^{-4}$ S/cm) but low σ_{yy} ($\approx 1.96 \times 10^{-6}$ S/cm), vice versa for a microstructure with rod fillers aligning along the y-axis. Such symmetric relation can be seen from the diagrams in Figure 4a,b. Furthermore, the rod can expand laterally to penetrate the sample in the other in-plane axis (forming a 2−3 type microstructure, see the third image in Figure 4c) and can eventually span the entire xy plane to form a multilayered 2−2 type microstructure. Such multilayered microstructures have the highest volume fraction of the lateral interfaces among all microstructures generated. Thus, they show the highest in-plane effective ion conductivity σ_{xx} and σ_{yy} (see Figure 4a,b), although their out-of-plane effective ion conductivity σ_{zz} is negligibly small.

4. CONCLUSIONS

We have developed a phase-field method based multiscale model that can be used to generate the microstructure pattern and predict the effective ion conductivity σ_{eff} of two-phase heterogeneous solid electrolytes. In the present multiscale model, the phase-field simulation is informed by DFT calculations to include the effects of the interface structural features (width and energy) on microstructure morphology and informs the calculation of the σ_{eff}. In contrast, such structural features of interfaces, although critically determining the interface ion conductivity and the microstructure morphology, were not considered during microstructure generation in previous computational models of heterogeneous solid electrolytes.[10,20−26]

A nanoporous β-Li_3PS_4 electrolyte has been chosen as an example of two-phase heterogeneous solid electrolyte. On the basis of the DFT-calculated surface depth and surface energy of the β-Li_3PS_4, we have generated nanoporous microstructures of different connectivity patterns, where the average pore size (~40 nm) in a 3−3 type pattern (Figure 1e) is close to experimental value (~30 nm). Furthermore, on the basis of the DFT-estimated surface Li-ion conductivity (3.14×10^{-3} S/cm) and experimentally measured bulk Li-ion conductivity in dense β-Li_3PS_4 (8.93×10^{-7} S/cm), we calculated room-temperature σ_{eff} of these nanoporous microstructure patterns both numerically and analytically. When porosity approaches the percolation threshold of these two-phase microstructure patterns, both numerical and analytical calculations predict that the σ_{eff} in nanoporous β-Li_3PS_4 (1.74×10^{-4} S/cm) is almost 3 orders of magnitude larger than that in dense counterparts and is in good agreement with experimental data (1.64×10^{-4} S/cm). The enhancement of σ_{eff} due to the formation of a 3D percolating ion-conducting surface network in the microstructure, demonstrated herein, is analogous to the reported enhancement of bulk Li-ion conductivity σ_{bulk} due to the formation of percolating ion-conducting pathways within

DOI: 10.1021/acsami.7b11202

the bulk lattice of a crystal.[64,76−78] Furthermore, we expect our findings to be generally applicable to other Li-ion conductors because diffusion along surfaces is in general faster than that in bulk due to the space-charge-induced ion-accumulation at surfaces.[60] Specifically, we expect that a porous $Li_{10}GeP_2S_{12}$ (LGPS)-type conductor with a 3D percolating ion-conducting surface network in its microstructure should possess much higher Li-ion conductivity than that in its dense counterpart. This will be exciting because the dense LGPS-type conductor already exhibits an ultrahigh Li-ion conductivity up to 2.5×10^{-2} S/cm at 25 °C.[78]

We have also utilized such phase-field based multiscale model to discover, in general, the relationship between microstructure patterns and σ_{eff} in two-phase solid electrolytes that involve ion-insulating fillers but highly conductive interfaces. This was achieved by generating a microstructure data set consisting of 1600 3D microstructure of different phase morphologies and the corresponding data set of σ_{eff}. The present multiscale model can also be employed to predict the microstructure and the corresponding effective properties of two-phase solid electrolytes involving ion-conducting second-phase fillers and possibly more ion-conductive interfaces.

Overall, the present phase-field based multiscale model, which closely integrates the first-principles DFT calculations, phase-field simulations, and effective medium theories, can be generally used to generate data sets of two-phase microstructure and corresponding effective material properties. These data sets will be useful to the data-driven mesoscale computational design of heterogeneous solid electrolytes.

■ ASSOCIATED CONTENT

Supporting Information

The Supporting Information is available free of charge on the ACS Publications website at DOI: 10.1021/acsami.7b11292.

First-principles calculations of the structural parameters of β-Li_3PS_4; surface energy of β-Li_3PS_4; activation energy of bulk and surface Li-ion diffusion in β-Li_3PS_4; surface volume fraction versus porosity for the microstructure patterns generated by phase-field simulations (PDF)

■ AUTHOR INFORMATION

Corresponding Author

*E-mail: juh34@psu.edu.

ORCID

Jia-Mian Hu: 0000-0002-7579-6440

Yi Wang: 0000-0001-6154-945X

Author Contributions

J.-M.H. and L.-Q.C. initiated the project. L.-Q.C. supervised the project. J.-M.H. designed the structure of the manuscript and performed the phase-field simulations and effective medium theories calculations. B.W. performed the first-principles DFT calculations using feedback from Y.W. and contributed to the writing of relevant content in the manuscript. Y.J. developed the code for microstructure generation through phase separation and contributed to the writing of the relevant Methods section. T.Y. developed the code for the numerical calculation of effective ion conductivity. X.C. helped with the statistical analyses of the generated microstructure patterns. J.-M.H. wrote the manuscript using feedback from B.W., Y.J., and L.-Q.C. J.-M.H. and B.W. contributed equally to this manuscript.

Notes

The authors declare no competing financial interest.

■ ACKNOWLEDGMENTS

The work is supported by National Science Foundation (NSF) with Grant Nos. of DMR-1410714 & DMR-1629270 (J.-M.H., B.W., T.Y., and L.-Q.C.), the U.S. Department of Energy, Office of Basic Energy Sciences, Division of Materials Sciences and Engineering, under Award DE-FG02-07ER46417 (X.C. and L.-Q.C.), and the Hamer Professorship (Y.J., Y.W., and L.-Q.C.).

■ REFERENCES

(1) Takada, K. Progress and Prospective of Solid-State Lithium Batteries. *Acta Mater.* **2013**, *61*, 759−770.

(2) Ren, Y.; Chen, K.; Chen, R.; Liu, T.; Zhang, Y.; Nan, C.-W. Oxide Electrolytes for Lithium Batteries. *J. Am. Ceram. Soc.* **2015**, *98*, 3603−3623.

(3) Kim, J. G.; Son, B.; Mukherjee, S.; Schuppert, N.; Bates, A.; Kwon, O.; Choi, M. J.; Chung, H. Y.; Park, S. A Review of Lithium and Non-Lithium Based Solid State Batteries. *J. Power Sources* **2015**, *282*, 299−322.

(4) Choi, J. W.; Aurbach, D. Promise and Reality of Post-Lithium-Ion Batteries with High Energy Densities. *Nat. Rev. Mater.* **2016**, *1*, 16013.

(5) Hu, Y.-S. Batteries: Getting Solid. *Nat. Energy* **2016**, *1*, 16042.

(6) Manthiram, A.; Yu, X.; Wang, S. Lithium Battery Chemistries Enabled by Solid-State Electrolytes. *Nat. Rev. Mater.* **2017**, *2*, 16103.

(7) Goodenough, J. B. Batteries and a Sustainable Modern Society. *Electrochem. Soc. Interface* **2016**, *25*, 67−70.

(8) Liu, W.; Liu, N.; Sun, J.; Hsu, P.-C.; Li, Y.; Lee, H.-W.; Cui, Y. Ionic Conductivity Enhancement of Polymer Electrolytes with Ceramic Nanowire Fillers. *Nano Lett.* **2015**, *15*, 2740−2745.

(9) Fu, K.; Gong, Y.; Dai, J.; Gong, A.; Han, X.; Yao, Y.; Wang, C.; Wang, Y.; Chen, Y.; Yan, C.; Li, Y.; Wachsman, E. D.; Hu, L. Flexible, Solid-State, Ion-Conducting Membrane with 3D Garnet Nanofiber Networks for Lithium Batteries. *Proc. Natl. Acad. Sci. U. S. A.* **2016**, *113*, 7094−7099.

(10) Liu, W.; Lee, S. W.; Lin, D.; Shi, F.; Wang, S.; Sendek, A. D.; Cui, Y. Enhancing Ionic Conductivity in Composite Polymer Electrolytes with Well-Aligned Ceramic nanowires. *Nat. Energy* **2017**, *2*, 17035.

(11) Zhai, H.; Xu, P.; Ning, M.; Cheng, Q.; Mandal, J.; Yang, Y. A Flexible Solid Composite Electrolyte with Vertically Aligned and Connected Ion-Conducting Nanoparticles for Lithium Batteries. *Nano Lett.* **2017**, *17*, 3182−3187.

(12) Liang, C. C. Conduction Characteristics of the Lithium Iodide-Aluminum Oxide Solid Electrolytes. *J. Electrochem. Soc.* **1973**, *120*, 1289−1292.

(13) Dudney, N. J. Composite Electrolytes. *Annu. Rev. Mater. Sci.* **1989**, *19*, 103−120.

(14) Croce, F.; Appetecchi, G. B.; Persi, L.; Scrosati, B. Nanocomposite Polymer Electrolytes for Lithium Batteries. *Nature* **1998**, *394*, 456−458.

(15) Nan, C.-W.; Fan, L.; Lin, Y.; Cai, Q. Enhanced Ionic Conductivity of Polymer Electrolytes Containing Nanocomposite SiO_2 Particles. *Phys. Rev. Lett.* **2003**, *91*, 266104.

(16) Roling, B.; Murugavel, S. Bulk and Interfacial Ionic Conduction in $LiAlSiO_4$ Glass Ceramics Containing Nano- and Microcrystallites. *Z. Phys. Chem.* **2005**, *219*, 23−33.

(17) Schirmeisen, A.; Taskiran, A.; Fuchs, H.; Bracht, H.; Murugavel, S.; Roling, B. Fast Interfacial Ionic Conduction in Nanostructured Glass Ceramics. *Phys. Rev. Lett.* **2007**, *98*, 225901.

(18) Li, C.; Gu, L.; Maier, J. Enhancement of the Li Conductivity in LiF by Introducing Glass/Crystal Interfaces. *Adv. Funct. Mater.* **2012**, *22*, 1145−1149.

(19) Liu, Z.; Fu, W.; Payzant, E. A.; Yu, X.; Wu, Z.; Dudney, N. J.; Kiggans, J.; Hong, K.; Rondinone, A. J.; Liang, C. Anomalous High Ionic Conductivity of Nanoporous β-Li_3PS_4. *J. Am. Chem. Soc.* **2013**, *135*, 975−978.

(20) Bunde, A.; Dieterich, W.; Roman, E. Dispersed Ionic Conductors and Percolation Theory. *Phys. Rev. Lett.* **1985**, *55*, 5−8.
(21) Roman, H. E.; Bunde, A.; Dieterich, W. Conductivity of Dispersed Ionic Conductors: A Percolation Model with Two Critical Points. *Phys. Rev. B: Condens. Matter Mater. Phys.* **1986**, *34*, 3439−3445.
(22) Blender, R.; Dieterich, W. A Random AC Network Model for Dispersed Ionic Conductors. *J. Phys. C: Solid State Phys.* **1987**, *20*, 6113.
(23) Roman, H. E.; Yussouff, M. Particle-Size Effect on the Conductivity of Dispersed Ionic Conductors. *Phys. Rev. B: Condens. Matter Mater. Phys.* **1987**, *36*, 7285−7288.
(24) Debierre, J.-M.; Knauth, P.; Albinet, G. Enhanced Conductivity in Ionic Conductor-Insulator Composites: Experiments and Numerical Model. *Appl. Phys. Lett.* **1997**, *71*, 1335−1337.
(25) Kalnaus, S.; Sabau, A. S.; Newman, S.; Tenhaeff, W. E.; Daniel, C.; Dudney, N. J. Effective Conductivity of Particulate Polymer Composite Electrolytes Using Random Resistor Network Method. *Solid State Ionics* **2011**, *199*−*200*, 44−53.
(26) Kalnaus, S.; Tenhaeff, W. E.; Sakamoto, J.; Sabau, A. S.; Daniel, C.; Dudney, N. J. Analysis of Composite Electrolytes with Sintered Reinforcement Structure for Energy Storage Applications. *J. Power Sources* **2013**, *241*, 178−185.
(27) Kohn, W.; Sham, L. J. Self-Consistent Equations Including Exchange and Correlation Effects. *Phys. Rev.* **1965**, *140*, A1133−A1138.
(28) Kresse, G.; Furthmüller, J. Efficient Iterative Schemes for ab initio Total-Energy Calculations Using a Plane-Wave Basis Set. *Phys. Rev. B: Condens. Matter Mater. Phys.* **1996**, *54*, 11169−11186.
(29) Blöchl, P. E. Projector Augmented-Wave Method. *Phys. Rev. B: Condens. Matter Mater. Phys.* **1994**, *50*, 17953−17979.
(30) Perdew, J. P.; Wang, Y. Accurate and Simple Analytic Representation of the Electron-Gas Correlation Energy. *Phys. Rev. B: Condens. Matter Mater. Phys.* **1992**, *45*, 13244−13249.
(31) Lepley, N. D.; Holzwarth, N. A. W.; Du, Y. A. Structures, Li^+ Mobilities, and Interfacial Properties of Solid Electrolytes Li_3PS_4 from First Principles. *Phys. Rev. B: Condens. Matter Mater. Phys.* **2013**, *88*, 104103.
(32) Monkhorst, H. J.; Pack, J. D. Special Points for Brillouin-Zone Integrations. *Phys. Rev. B: Condens. Matter Mater. Phys.* **1976**, *13*, 5188−5192.
(33) Du, Y. A.; Holzwarth, N. A. W. First-Principles Study of LiPON and Related Solid Electrolytes. *Phys. Rev. B: Condens. Matter Mater. Phys.* **2010**, *81*, 184106.
(34) Holzwarth, N. A. W.; Lepley, N. D.; Du, Y. A. Computer Modeling of Lithium Phosphate and Thiophosphate Electrolyte Materials. *J. Power Sources* **2011**, *196*, 6870−6876.
(35) Henkelman, G.; Jónsson, H. Improved Tangent Estimate in the Nudged Elastic Band Method for Finding Minimum Energy Paths and Saddle Points. *J. Chem. Phys.* **2000**, *113*, 9978−9985.
(36) Homma, K.; Yonemura, M.; Kobayashi, T.; Nagao, M.; Hirayama, M.; Kanno, R. Crystal Structure and Phase Transitions of the Lithium Ionic Conductor Li_3PS_4. *Solid State Ionics* **2011**, *182*, 53−58.
(37) Yang, Y.; Wu, Q.; Cui, Y.; Chen, Y.; Shi, S.; Wang, R.-Z.; Yan, H. Elastic Properties, Defect Thermodynamics, Electrochemical Window, Phase Stability, and Li^+ Mobility of Li_3PS_4: Insights from First-Principles Calculations. *ACS Appl. Mater. Interfaces* **2016**, *8*, 25229−25242.
(38) Chen, L. Q. Phase-Field Models for Microstructure Evolution. *Annu. Rev. Mater. Res.* **2002**, *32*, 113−140.
(39) Wang, T.; Sheng, G.; Liu, Z.-K.; Chen, L.-Q. Coarsening Kinetics of γ' Precipitates in the Ni−Al−Mo System. *Acta Mater.* **2008**, *56*, 5544−5551.
(40) Yadav, A. K.; Nelson, C. T.; Hsu, S. L.; Hong, Z.; Clarkson, J. D.; Schlepütz, C. M.; Damodaran, A. R.; Shafer, P.; Arenholz, E.; Dedon, L. R.; Chen, D.; Vishwanath, A.; Minor, A. M.; Chen, L. Q.; Scott, J. F.; Martin, L. W.; Ramesh, R. Observation of Polar Vortices in Oxide Superlattices. *Nature* **2016**, *530*, 198−201.
(41) Cahn, J. W.; Hilliard, J. E. Free Energy of a Nonuniform System. I. Interfacial Free Energy. *J. Chem. Phys.* **1958**, *28*, 258−267.
(42) Provatas, N.; Elder, K. *Phase-Field Methods in Materials Science and Engineering*; Wiley: Weinheim, 2011.
(43) Cahn, J. W. Free Energy of a Nonuniform System. II. Thermodynamic Basis. *J. Chem. Phys.* **1959**, *30*, 1121−1124.
(44) Brunini, V. E.; Schuh, C. A.; Carter, W. C. Percolation of Diffusionally Evolved Two-Phase Systems. *Phys. Rev. E: Stat. Phys., Plasmas, Fluids, Relat. Interdiscip. Top.* **2011**, *83*, 021119.
(45) Zhu, J.; Chen, L.-Q.; Shen, J.; Tikare, V. Coarsening Kinetics from a Variable-Mobility Cahn-Hilliard Equation: Application of a Semi-Implicit Fourier Spectral Method. *Phys. Rev. E: Stat. Phys., Plasmas, Fluids, Relat. Interdiscip. Top.* **1999**, *60*, 3564−3572.
(46) Sheng, G.; Wang, T.; Du, Q.; Wang, K.; Liu, Z.; Chen, L. Coarsening Kinetics of a Two Phase Mixture with Highly Disparate Diffusion Mobility. *CiCP* **2010**, *8*, 249−264.
(47) Herring, C. The Use of Classical Macroscopic Concepts in Surface-Energy Problems. In *Structure and Properties of Solid Surfaces*; Proceedings of a conference arranged by the National Research Council, September 1952, Lake Geneva, WI; Gomer, R., Smith, C. S., Eds.; University of Chicago Press: Chicago, IL, 1953.
(48) Simmons, J.; Shen, C.; Wang, Y. Phase Field Modeling of Simultaneous Nucleation and Growth by Explicitly Incorporating Nucleation Events. *Scr. Mater.* **2000**, *43*, 935−942.
(49) Hu, S. Y.; Chen, L. Q. A Phase-Field Model for Evolving Microstructures with Strong Elastic Inhomogeneity. *Acta Mater.* **2001**, *49*, 1879−1890.
(50) Wang, J. J.; Ma, X. Q.; Li, Q.; Britson, J.; Chen, L.-Q. Phase Transitions and Domain Structures of Ferroelectric Nanoparticles: Phase Field Model Incorporating Strong Elastic and Dielectric Inhomogeneity. *Acta Mater.* **2013**, *61*, 7591−7603.
(51) Stoneham, A. M.; Wade, E.; Kilner, J. A. A Model for the Fast Ionic Diffusion in Alumina-Doped Lii. *Mater. Res. Bull.* **1979**, *14*, 661−666.
(52) Nan, C.-W. Conduction Theory of Ionic Conductor Containing Dispersed Second Phase. *Acta. Phys. Sin.* **1987**, *36*, 191−198.
(53) Roman, H. E. A Continuum Percolation Model for Dispersed Ionic Conductors. *J. Phys.: Condens. Matter* **1990**, *2*, 3909.
(54) Nan, C.-W.; Smith, D. M. A.C. Electrical Properties of Composite Solid Electrolytes. *Mater. Sci. Eng., B* **1991**, *10*, 99−106.
(55) Kalnaus, S.; Sabau, A. S.; Tenhaeff, W. E.; Dudney, N. J.; Daniel, C. Design of Composite Polymer Electrolytes for Li Ion Batteries Based on Mechanical Stability Criteria. *J. Power Sources* **2012**, *201*, 280−287.
(56) McLachlan, D. S.; Blaszkiewicz, M.; Newnham, R. E. Electrical Resistivity of Composites. *J. Am. Ceram. Soc.* **1990**, *73*, 2187−2203.
(57) Verkerk, M. J.; Middelhuis, B. J.; Burggraaf, A. J. Effect of Grain Boundaries on the Conductivity of High-Purity ZrO_2-Y_2O_3 Ceramics. *Solid State Ionics* **1982**, *6*, 159−170.
(58) Hwang, J.-H.; McLachlan, D. S.; Mason, T. O. Brick Layer Model Analysis of Nanoscale-to-Microscale Cerium Dioxide. *J. Electroceram.* **1999**, *3*, 7−16.
(59) Abrantes, J. C. C.; Labrincha, J. A.; Frade, J. R. Applicability of the Brick Layer Model to Describe the Grain Boundary Properties of Strontium Titanate Ceramics. *J. Eur. Ceram. Soc.* **2000**, *20*, 1603−1609.
(60) Maier, J. Defect Chemistry and Conductivity Effects in Heterogeneous Solid Electrolytes. *J. Electrochem. Soc.* **1987**, *134*, 1524−1535.
(61) Chen, Y.; Cai, L.; Liu, Z.; dela Cruz, C. R.; Liang, C.; An, K. Correlation of Anisotropy and Directional Conduction in β-Li_3PS_4 Fast Li^+ Conductor. *Appl. Phys. Lett.* **2015**, *107*, 013904.
(62) Nernst, W. Zur Kinetik Der in Lösung Befindlichen Körper. *Z. Phys. Chem.* **1888**, *2*, 613.
(63) Philibert, J. *Atom Movements: Diffusion and Mass Transport in Solids*; Editions de Physique: Les Ulis, France, 1991.
(64) Phani Dathar, G. K.; Balachandran, J.; Kent, P. R. C.; Rondinone, A. J.; Ganesh, P. Li-Ion Site Disorder Driven Superionic

DOI: 10.1021/acsami.7b11202

Conductivity in Solid Electrolytes: A First-Principles Investigation of β-Li_3PS_4. *J. Mater. Chem. A* **2017**, *5*, 1153−1159.
(65) Tachez, M.; Malugani, J.-P.; Mercier, R.; Robert, G. Ionic Conductivity of and Phase Transition in Lithium Thiophosphate Li_3PS_4. *Solid State Ionics* **1984**, *14*, 181−185.
(66) Lee, S.; Zhang, W.; Khatkhatay, F.; Wang, H.; Jia, Q.; MacManus-Driscoll, J. L. Ionic Conductivity Increased by Two Orders of Magnitude in Micrometer-Thick Vertical Yttria-Stabilized ZrO_2 Nanocomposite Films. *Nano Lett.* **2015**, *15*, 7362−7369.
(67) Yang, S. M.; Lee, S.; Jian, J.; Zhang, W.; Lu, P.; Jia, Q.; Wang, H.; Won Noh, T.; Kalinin, S. V.; MacManus-Driscoll, J. L. Strongly Enhanced Oxygen Ion Transport through Samarium-Doped CeO_2 Nanopillars in Nanocomposite Films. *Nat. Commun.* **2015**, *6*, 8588.
(68) Wieczorek, W.; Such, K.; Florjanczyk, Z.; Stevens, J. R. Polyether, Polyacrylamide, $LiClO_4$ Composite Electrolytes with Enhanced Conductivity. *J. Phys. Chem.* **1994**, *98*, 6840−6850.
(69) Lin, D.; Liu, W.; Liu, Y.; Lee, H. R.; Hsu, P.-C.; Liu, K.; Cui, Y. High Ionic Conductivity of Composite Solid Polymer Electrolyte Via in Situ Synthesis of Monodispersed SiO_2 Nanospheres in Poly(Ethylene Oxide). *Nano Lett.* **2016**, *16*, 459−465.
(70) Yang, C.-M.; Kim, H.-S.; Na, B.-K.; Kum, K.-S.; Cho, B. W. Gel-Type Polymer Electrolytes with Different Types of Ceramic Fillers and Lithium Salts for Lithium-Ion Polymer Batteries. *J. Power Sources* **2006**, *156*, 574−580.
(71) Liu, Y.; Lee, J. Y.; Hong, L. Morphology, Crystallinity, and Electrochemical Properties of in Situ Formed Poly(Ethylene Oxide)/TiO_2 Nanocomposite Polymer Electrolytes. *J. Appl. Polym. Sci.* **2003**, *89*, 2815−2822.
(72) Croce, F.; Sacchetti, S.; Scrosati, B. Advanced, Lithium Batteries Based on High-Performance Composite Polymer Electrolytes. *J. Power Sources* **2006**, *162*, 685−689.
(73) Newnham, R. E.; Skinner, D. P.; Cross, L. E. Connectivity and Piezoelectric-Pyroelectric Composites. *Mater. Res. Bull.* **1978**, *13*, 525−536.
(74) Sata, N.; Eberman, K.; Eberl, K.; Maier, J. Mesoscopic Fast Ion Conduction in Nanometre-Scale Planar Heterostructures. *Nature* **2000**, *408*, 946−949.
(75) Ji, Y.-Z.; Wang, Z.; Wang, B.; Chen, Y.; Zhang, T.; Chen, L.-Q.; Song, X.; Chen, L. Effect of Meso-Scale Geometry on Piezoelectric Performances of Additively Manufactured Flexible Polymer-Pb-$(Zr_xTi_{1-x})O_3$ Composites. *Adv. Eng. Mater.* **2017**, *19*, 1600803.
(76) Wang, Y.; Richards, W. D.; Ong, S. P.; Miara, L. J.; Kim, J. C.; Mo, Y.; Ceder, G. Design Principles for Solid-State Lithium Superionic Conductors. *Nat. Mater.* **2015**, *14*, 1026−31.
(77) Ma, C.; Cheng, Y.; Chen, K.; Li, J.; Sumpter, B. G.; Nan, C.-W.; More, K. L.; Dudney, N. J.; Chi, M. Mesoscopic Framework Enables Facile Ionic Transport in Solid Electrolytes for Li Batteries. *Adv. Energy Mater.* **2016**, *6*, 1600053.
(78) Kato, Y.; Hori, S.; Saito, T.; Suzuki, K.; Hirayama, M.; Mitsui, A.; Yonemura, M.; Iba, H.; Kanno, R. High-Power All-Solid-State Batteries Using Sulfide Superionic Conductors. *Nat. Energy* **2016**, *1*, 16030.

DOI: 10.1021/acsami.7b11202